



# Fully automated geometric feature analysis in optical coherence tomography angiography for objective classification of diabetic retinopathy

DAVID LE,<sup>1,4</sup> MINHAJ ALAM,<sup>1,4</sup> BERNADETTE A. MIAO,<sup>2</sup> JENNIFER I. LIM,<sup>3</sup>  
AND XINCHENG YAO<sup>1,3,5</sup>

<sup>1</sup>Department of Bioengineering, University of Illinois at Chicago, Chicago, IL 60607, USA

<sup>2</sup>Benet Academy, Lisle, IL, 60532, USA

<sup>3</sup>Department of Ophthalmology and Visual Sciences, University of Illinois at Chicago, Chicago, IL 60612, USA

<sup>4</sup>These authors contributed equally to this work

<sup>5</sup>[xcy@uic.edu](mailto:xcy@uic.edu)

**Abstract:** This study is to establish quantitative features of vascular geometry in optical coherence tomography angiography (OCTA) and validate them for the objective classification of diabetic retinopathy (DR). Six geometric features, including total vessel branching angle (VBA:  $\theta$ ), child branching angles (CBAs:  $\alpha_1$  and  $\alpha_2$ ), vessel branching coefficient (VBC), and children-to-parent vessel width ratios (VWR1 and VWR2), were automatically derived from each vessel branch in OCTA. Comparative analysis of healthy control, diabetes with no DR (NoDR), and non-proliferative DR (NPDR) was conducted. Our study reveals four quantitative OCTA features to produce robust DR detection and staging classification: (ANOVA,  $P < 0.05$ ), VBA, CBA1, VBC, and VWR1.

© 2019 Optical Society of America under the terms of the [OSA Open Access Publishing Agreement](#)

## 1. Introduction

Diabetic retinopathy (DR), a major microvascular complication of diabetes mellitus (DM) and a preventable blindness around the world [1], is predicted to significantly increase in prevalence worldwide. By the year 2030, the number of people diagnosed with DM is predicted to reach 552 million [2] and nearly 45% of DM patients may develop DR associated vision impairment [1]. Early detection of DR is paramount to prevention of progression and essential to prevent vision loss [2].

According to Murray's principle [3], the retinal vascular network and its branching pattern develop in such a way that the shear stress and energy required for efficient blood flow (and oxygen) across the system are minimized. Any alteration from an optimal branching network in the retina will result in increased shear stress, impaired microcirculatory support, and reduced efficiency of the blood-oxygen flow, increasing the risk of vascular damage [4]. The functional impairment caused by DM leads to such alterations in blood flow and in the vessel wall structures which in turn affect the endothelium and blood retinal barriers [5,6]. These changes are believed to affect the vascular geometry of the retina, even before mild non-proliferative DR (NPDR) is detectable. Therefore, geometric features for quantifying retinal vascular abnormalities hold promise to identify very early diabetic retinopathy as well as progression of DR. As these features are non-dimensional, the effects of optical artifacts, refractive errors, and variation of image resolutions are minimized.

Several recent studies have explored geometric biomarkers in the retina for evaluating DR [7–14] and other systemic complications [15]. However, the investigated features were somewhat limited and did not provide indications on how the geometry of retinal vasculature changed within each patient during DR progression [16,17]. Additionally, the process of

measuring the different features was not automatic and required manual input from ophthalmologists. There are very few prospective studies where the geometric features were used to predict subsequent DR and associated change in retinal vascular geometry [18–20]. A major limitation of previous studies of geometric features is that they relied on fundus imaging for quantifying the DR induced abnormalities. While fundus photography provides qualitative information and is widely used for observing microaneurysms and exudates, it has limited ability for providing quantitative representation of microvascular architecture of the retina [21]. This is particularly true for the smaller parafoveal capillary structures for which geometric distortions cannot be captured using fundus photography [22–24]. Since most of the geometric changes occur within the parafoveal capillary network, it is essential to quantify the geometric features in that area in order to identify early onset DR and evaluate its progression. An alternative imaging option is optical coherence tomography angiography (OCTA) which provides depth-resolved visualization of multiple retinal layers with high-resolution even in the capillary level at the foveal region.

## 2. Materials and methods

The detailed methodology of the geometric feature analysis is described in this section. As illustrated in Fig. 1(a), the core steps are divided into three main sections: preprocessing, branch triangle identification, and quantification of geometric features. Furthermore, the algorithm used for geometric feature measurement is illustrated in Fig. 1(b).

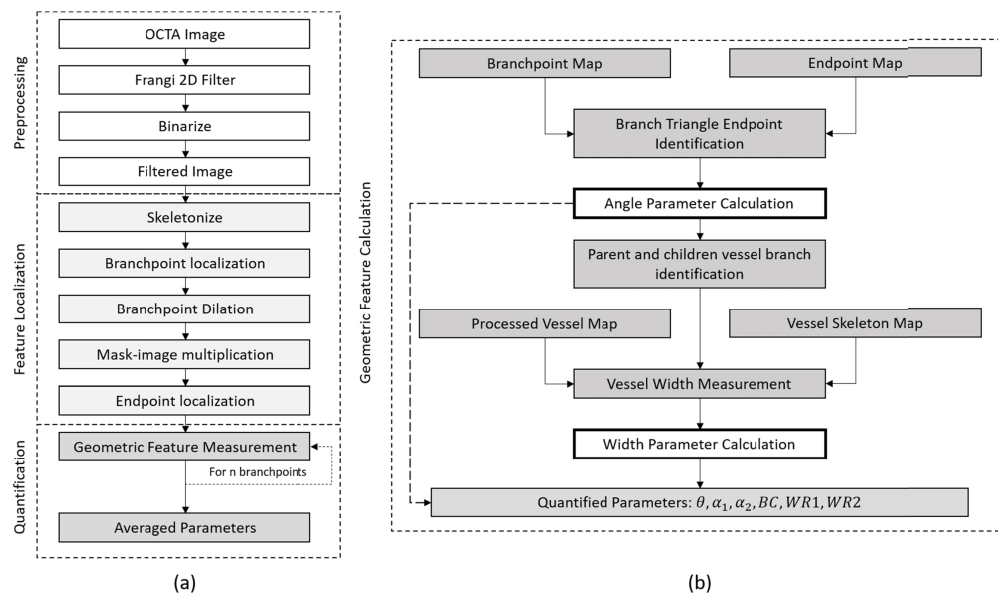


Fig. 1. (a) Core steps of geometric feature analysis, (b) geometric feature measurement algorithm to quantify the features for n number of branchpoints, where the thick boxes represent outputs of the algorithm.

### 2.1 Data acquisition

This study was approved by the institutional review board of the University of Illinois at Chicago and follows the ethical standards stated in the Declaration of Helsinki. Healthy controls, diabetic patients with no DR (NoDR) and DR were recruited from the University of Illinois at Chicago (UIC) Retinal Clinic. Every subject underwent optical coherence tomography (OCT) and OCT-angiography (OCTA) imaging of both eyes. DR patients were classified based on severity (mild, moderate, and severe) according to the Early Treatment

Diabetic Retinopathy Study of staging system. Grading was performed by a retina specialist, utilizing a slit-lamp fundus lens.

All OCTA data were acquired using an ANGIOVUE spectral domain OCTA system (Optovue, Fremont, CA), with a 70-kHz A-scan rate, an axial resolution of 5  $\mu\text{m}$ , and a lateral resolution of 15  $\mu\text{m}$ . All OCTA images were macular scans and had a field of view of 6 mm by 6 mm. OCTA images were exported using the ReVue (Optovue) software. Custom-developed MATLAB (Mathworks, Natick, MA) procedures were used for further image analysis, feature extraction, and image classification.

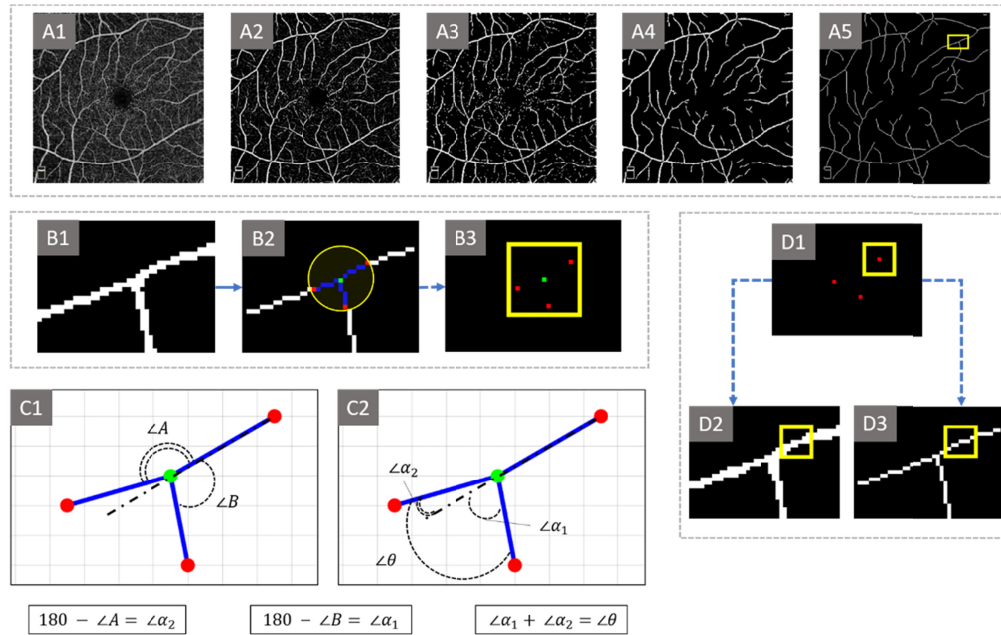


Fig. 2. (A) Illustration of preprocessing steps. (A1) Input OCTA image, (A2) Frangi 2D filtered image, (A3) binarized image, (A4) processed vessel map, and (A5) skeleton map. (B) The feature localization step for an example branchpoint. (B1) Processed vessel map, (B2) a composite image containing the vessel skeleton, where the green pixel represents the branchpoint, red pixels represent the end points, the blue pixels represent our vessels of interest, and the yellow circle represents the dilated area. (B3) A composite image of the branchpoint (green) and endpoint (red), where the yellow square represents the window area. (C). Illustration of branch angle measurement. Angles A and B in the C1 are complementary angles used to calculate  $\theta$ ,  $\alpha_1$ , and  $\alpha_2$  in the C2. (D). Illustration of window method used to calculate vessel width of one representative vessel branch. (D1) A yellow window is centered around an endpoint (the red pixel). The coordinates of the yellow window in (D1) are used to measure the pixels in the processed vessel map (D2), and the skeleton map (D3).

## 2.2 Preprocessing

The first core step is image preprocessing, as illustrated in Fig. 2(A). For an input OCTA image (Fig. 2(A1)), we first filter the image using the Frangi 2D filter (Fig. 2(A2)). The Frangi 2D Filter is used to enhance vessel edges in the input image. After enhancing the blood vessel edges, the resulting image is binarized (Fig. 2(A3)). The binarized image is then filtered using MATLAB morphological functions to remove spurs and unwanted pixels. The resulting image is referred to as the processed vessel map (Fig. 2(A4)). The corresponding skeleton vessel map is shown in Fig. 2(A5).

## 2.3 Feature extraction

Using the preprocessed OCTA images, we can begin feature localization and quantification. In this study, we propose six geometric features for quantitative analysis of DR staging using

a fully automated algorithm. These features can be divided into two subcategories, vessel angle-based and vessel width-based geometric features.

Vessel angle-based features measure the degree of bifurcation and relative angle change among the parent and child vessel branches. The first feature is vessel branching angle (VBA:  $\theta$ ), which measures the overall degree of bifurcation between the child branches. The second and third features are the child branching angle 1 (CBA1:  $\alpha_1$ ) and child branching angle 2 (CBA2:  $\alpha_2$ ), which measures the direction of branching of each child vessel. The child angles can provide information relating to the deviation of direction of child vessels with respect to the original parent vessel direction.

Vessel width-based features measure the structural change of the vessels as a result of branching. The first vessel-width feature is vessel branching coefficient (VBC), which measures the effect of branching on vessel area between the parent, first (larger) child, and second (smaller) child. Similarly, the second and third vessel-width features are vessel width ratio 1 (VWR1) and width ratio 2 (VWR2), which examines the change in width between individual child and parent vessels.

### 2.3.1 Branching triangle identification

In this step, the processed vessel map is used to extract the vessel skeleton, branch points, and end points. Figure 2(B) illustrates the steps for locating branch points and corresponding endpoints. Figure 2(B1) is one branch point from Fig. 2(A4) (marked by the yellow rectangle in Fig. 2(A5)).

First, the vessel skeleton map is extracted from the processed vessel map. Next, the vessel branchpoints are determined from the vessel skeleton using morphological functions (Fig. 2(B1)). The branchpoints indicate where vessel branching occurs. Furthermore, we can utilize the branchpoints to create a mask to extract the region of interest (Fig. 2(B2)). In this study, the region of interest is referred to as branch triangles. The method of masking starts by dilating each branchpoint. Based on empirical trials, a dilation radius of 5 pixels is large enough to encompass the region of interest, and small enough to not overlap with adjacent branchpoints. The newly created mask is then multiplied with the skeleton map to generate an image containing the individual branch triangles. The branch triangle visualization is referenced as the colored pixels in Fig. 2(B2). In the last step the endpoints of each branch triangles are extracted into a separate image (Fig. 2(B3)). The preprocessing and branch triangle identification steps results in four images, i.e., the processed vessels, vessel skeleton, branchpoints, and endpoints, used for following feature measurement.

### 2.3.2 Quantification of features

The inputs into the fully automated algorithm are the processed vessel, vessel skeleton, branchpoint, and endpoint images. The algorithm is illustrated in Fig. 1(b) and runs iteratively for each branchpoint in the image. The algorithm is designed to quantify each branchpoint with exactly 3 endpoints. For the point that is crossed by two large vessels, the corresponding number of endpoints will be 4, and therefore is excluded from quantitative branchpoint analysis.

For a branchpoint, the first step is the branch triangle endpoint identification by a window method illustrated in Fig. 2(B3). For this process, the window area is centered at the branchpoint, and the window is a square whose width is 15 pixels. The width size is dependent on the dilation radius used in the branch triangle identification step. If the window is too small, then none of the endpoints would be detected. Similarly, if the width is too large, then the endpoints of other branches would be detected. The window method records the coordinates of each endpoint of the branch triangles.

Next the recorded coordinates of the endpoints and branchpoints are used to create vectors of the vessels, resulting in a set of parent and two child vectors. From these three vectors, three angles, A and B (Fig. 2(C1)), and  $\theta$  (Fig. 2(C2)) are quantified (Fig. 1(b)). Based on the

physiology of vessel branching, the smallest one of these three angles is the VBA ( $\theta$ ). Using geometric identities, CBA1 ( $\alpha_1$ ) and CBA2 ( $\alpha_2$ ) are calculated from angle B and A, respectively, of the vessel, where CBA1 is larger than CBA2. We can then use the calculated angles ( $\theta$ ,  $\alpha_1$ ,  $\alpha_2$ ) to identify the parent and child vessels. The two vectors/endpoints that form the branching angle are identified as the child vessels, and the remaining vector/endpoint identifies the parent vessel.

By identifying the parent and child vessels, the width of each vessel is measured by using another window method. For this process, the window area is centered around each endpoint (Fig. 2(D1)). The coordinates of the window area are used to take the ratio of the sum of the of pixels in the processed vessel map (Fig. 2(D2)) to sum of the pixels in the vessel skeleton map (Fig. 2(D3)). This ratio defines the width of the vessel segment. The window method is repeated for all parent and child vessels.

The values of the widths are then used to calculate the width parameters, VBC, VWR1, and VWR2. The width parameters are summarized in equations Table 1, respectively. The output of the algorithm are the angle-based features, VBA ( $\theta$ ), CBA1 ( $\alpha_1$ ), CBA 2 ( $\alpha_2$ ), and the width-based features, VBC, VWR1, VWR2. The algorithm runs iteratively for each identified branchpoints in an OCTA image. In the final step, the features are averaged and reported.

**Table 1. Quantitative Geometric Features**

Geometric Parameter	Measurement
VBA ( $\theta$ )	$\angle \theta = 360^\circ - \angle A - \angle B$ <p>Where:  <math>\angle A</math> is the largest angle.  <math>\angle B</math> is the second largest angle.</p>
CBA1 ( $\alpha_1$ )	$\angle \alpha_1 = 180^\circ - \angle B$
CBA2 ( $\alpha_2$ )	$\angle \alpha_2 = 180^\circ - \angle A$
VBC	$VBC = \frac{(child_1 \text{ width})^2 + (child_2 \text{ width})^2}{(parent \text{ width})^2}$ <p>Where:</p> $vessel \text{ width} = \frac{\sum_{i=1, j=1}^n B(i, j)}{\sum_{i=1, j=1}^n S(i, j)}$ <p>B(i,j) represents the pixels occupied by the windowed vessel map, and S(i,j) represents the pixels occupied by the windowed vessel skeleton.</p>
VWR1	$VWR1 = \frac{child_1 \text{ width}}{parent \text{ width}}$
VWR2	$VWR2 = \frac{child_2 \text{ width}}{parent \text{ width}}$

## 2.4 Statistical analysis

The statistical analyses were performed using MATLAB (MathWorks, Natick, MA) and Microsoft Excel (Microsoft Corporation, Redmond, WA). All quantitative geometric features for different groups were compared using one-way, multi-label analysis of variance (ANOVA) to compare difference in mean values of the features among multiple groups. Following ANOVA, one versus one comparisons of the features between control, NoDR and NPDR stages (mild, moderate and severe) were performed using a Student *t*-test, with statistical significance was defined with a *P* value < 0.05.

## 3. Results

Our OCTA image database consisted of 120 OCTA images from 60 NPDR patients, 24 OCTA images of 17 NoDR patients, and 40 images from 20 control subjects. We excluded 6



eyes due to poor OCTA images and another 4 eyes due to presence of other retinal diseases. Among the NPDR OCTAs, there were 20 sets each of mild, moderate, and severe NPDR (40 OCTAs for each stage). There was no statistical significance in the distribution of age, sex and hypertension between control and DR groups. (ANOVA,  $P = 0.14$ ; chi-square test,  $P = 0.11$  and  $P = 0.32$ , respectively). The demographics of our studied subjects are detailed in Table 2.

**Table 2. Demographics of control and DR subjects**

			Diabetic Retinopathy		
	Control	NoDR	Mild NPDR	Moderate NPDR	Severe NPDR
Number of subjects	20	17	20	20	20
Sex (male)	12	6	11	12	11
Age (mean $\pm$ SD), years	42 $\pm$ 9.8	66.4 $\pm$ 10.14	50.1 $\pm$ 12.61	50.8 $\pm$ 8.39	57.84 $\pm$ 10.37
Age range, years	25-71	49 - 86	24-74	32-68	41-73
Duration of diabetes, (mean $\pm$ SD), years	-	-	19.64 $\pm$ 13.27	16.13 $\pm$ 10.58	23.40 $\pm$ 11.95
Diabetes Type (% type II)	-	100	100	100	100
Insulin dependent (Y/N)	-	14/3	7/13	12/8	15/5
HbA1C, %	-	5.9 $\pm$ 0.7	6.5 $\pm$ 0.6	7.3 $\pm$ 0.9	7.8 $\pm$ 1.3
HTN prevalence, %	10	17	45	80	80

<sup>a</sup> DR, diabetic retinopathy, SD, standard deviation, HbA1C, Glycated hemoglobin, HTN, hypertension

### 3.1 Geometric feature analysis

The detailed geometric feature analysis is summarized in Table 3. Among six geometric features of retinal vasculature in OCTA, VBA ( $\theta$ ), CBA1 ( $\alpha_1$ ), VBC, and VWR1 were the most sensitive to DR stages. The angle-based parameters, VBA ( $\theta$ ), CBA1 ( $\alpha_1$ ), and CBA2 ( $\alpha_2$ ) had positive correlation with severity of NPDR staging, while width-based parameters, VBC, VWR1, and VWR2, had negative correlation with severity of NPDR staging. In the case of control vs. NPDR, VBA ( $\theta$ ), CBA1 ( $\alpha_1$ ), and CBA2 ( $\alpha_2$ ) increased by 1.53%, 0.522%, and 4.05%, respectively (Student's t-test: no parameters had  $P < 0.05$ ). While for VBC, VWR1, and VWR2 decreased by 4.96%, 6.22%, and 1.93%, respectively (Student's t-test:  $P < 0.01$  for VBC and VWR1). The features, VBA ( $\theta$ ), CBA1 ( $\alpha_1$ ), VBC, and VWR1, were the only features able to differentiate control, NoDR, and individual NPDR groups (ANOVA,  $P < 0.05$ ).

Table 3. Statistics of geometric features in control and DR groups

Averaged Geometric Features $\pm$ std						
Parameters	Control	NoDR	Mild	Moderate	Severe	p-values
VBA ( $\theta$ )	$80.83 \pm 3.95$	$78.82 \pm 3.07$	$82.95 \pm 2.93$	$83.53 \pm 4.59$	$80.79 \pm 4.84$	0.002
CBA1 ( $\alpha_1$ )	$57.69 \pm 3.05$	$56.08 \pm 2.95$	$58.72 \pm 2.59$	$59.39 \pm 3.27$	$56.86 \pm 4.23$	0.011
CBA2 ( $\alpha_2$ )	$23.13 \pm 2.37$	$22.74 \pm 2.09$	$24.24 \pm 2.56$	$24.15 \pm 3.5$	$23.94 \pm 3.34$	0.280
VBC	$1.20 \pm 0.08$	$1.12 \pm 0.09$	$1.15 \pm 0.16$	$1.17 \pm 0.13$	$1.12 \pm 0.11$	0.032
VWR1	$0.641 \pm 0.06$	$0.610 \pm 0.05$	$0.604 \pm 0.06$	$0.604 \pm 0.07$	$0.598 \pm 0.06$	0.047
VWR2	$0.815 \pm 0.05$	$0.776 \pm 0.04$	$0.810 \pm 0.08$	$0.815 \pm 0.08$	$0.785 \pm 0.07$	0.086

Based on the ANOVA test, four features, i.e., VBA ( $\theta$ ), CBA1 ( $\alpha_1$ ), VBC, and VWR1, had significance for group differentiation. A post hoc test was conducted to determine which groups were significantly differentiable. In this study, we followed a two tailed t-test, where p-values less than 0.05 or 0.01 are significant, and p-values less than 0.001 are highly significant.

The individual t-test comparison for VBA ( $\theta$ ) is shown in Table 4. In the case of VBA ( $\theta$ ), control groups can be significantly differentiated from NoDR, mild, and moderate groups using individual t-test (Student's t-test:  $P < 0.05$  for control vs NoDR, mild, and moderate NPDR). NoDR groups can be highly significantly differentiated from mild, and moderate groups (Student's t-test:  $P < 0.001$  for NoDR vs mild, and moderate NPDR), and mild can be significantly differentiated from severe groups (Student's t-test:  $P < 0.05$  for mild vs severe NPDR).

Table 4. Results of student t-tests for individual group significance comparisons for branching angle, due to the significance of the ANOVA test.

Individual comparison t-test: VBA ( $\theta$ )					
	Control	NoDR	Mild	Moderate	Severe
Control					
NoDR	$<0.05$				
Mild	$<0.05$	$<0.001$			
Moderate	$<0.05$	$<0.001$	0.652		
Severe	0.975	0.063	$<0.05$	0.05	

The individual t-test comparison for CBA1 ( $\alpha_1$ ) is shown in Table 5. For CBA1 ( $\alpha_1$ ), NoDR groups can be significantly differentiated from mild, and moderate groups (Student's t-test:  $P < 0.01$  for NoDR vs mild, and moderate NPDR), while severe groups can be significantly differentiated from mild, and moderate groups (Student's t-test:  $P < 0.05$  for severe vs mild, and moderate NPDR).

**Table 5. Results of student t-tests for individual group significance comparisons for child branching angle 1, due to the significance of the ANOVA test.**

Individual comparison t-test: CBA1 ( $\alpha 1$ )					
	Control	NoDR	Mild	Moderate	Severe
Control					
NoDR	0.056				
Mild	0.211	<0.01			
Moderate	0.081	<0.01	0.496		
Severe	0.356	0.417	<0.05	<0.05	

The individual t-test comparison for VBC is shown in Table 6. In case of VBC, control groups can be significantly differentiated from NoDR and severe groups (Student's t-test:  $P < 0.01$  for control vs NoDR, and severe NPDR). No other groups can be differentiated from each other.

**Table 6. Results of student t-tests for individual group significance comparisons for vessel branching coefficient, due to the significance of the ANOVA test.**

Individual comparison t-test: VBC					
	Control	NoDR	Mild	Moderate	Severe
Control					
NoDR	<0.01				
Mild	0.185	0.51			
Moderate	0.446	0.136	0.571		
Severe	<0.01	0.994	0.519	0.144	

The individual t-test comparison for VWR1 is shown in Table 7. For VWR1, control groups can be significantly differentiated from NoDR, mild, and severe groups (Student's t-test  $P < 0.05$  for control vs NoDR, and mild NPDR, and  $P < 0.01$  for control vs severe NPDR). No other groups can be differentiated from each other.

**Table 7. Results of student t-tests for individual group significance comparisons for vessel width ratio 1, due to the significance of the ANOVA test.**

Individual comparison t-test: VWR1					
	Control	NoDr	Mild	Moderate	Severe
Control					
NoDR	<0.05				
Mild	<0.05	0.74			
Moderate	0.056	0.732	0.981		
Severe	<0.01	0.396	0.719	0.752	

#### 4. Discussion

In summary, we developed a fully automated method to quantify geometric features, including VBA, CBA1, CBA2, VBC, VWR1, and VWR2. Comparative OCTA analysis of healthy control, diabetes with NoDR and NPDR subjects were conducted.



As stated by Murray's principle, optimal blood flow transport is achieved with minimum energy and maximum vascular diffusion into surrounding tissue [3]. Changes to the vascular structures caused by DR and other diseases would decrease optimal transport of blood and nutrients. Therefore, quantitative geometric analysis can provide biomarkers for objective DR detection, progression monitoring, and treatment assessment. In this study, we quantified two categories of geometry, i.e., the angle (VBA, CBA1, CBA2) and width-based (VBC, VWR1, and VWR2) features, in OCTA.

In principle, the angle-based features can quantify abnormal changes in blood transport optimality in DR. Using traditional fundus photography, previous studies have observed widening of VBA associated with DR [15,25,26]. However, fundus photography has limited resolution and contrast to disclose subtle changes, particularly in the foveal area where the capillary structures are small, at early onset of mild DR [27]. Moreover, previous studies used manual or semi-manual marking software to analyze the geometric features, which was time consuming with labor intensive involvement of experienced ophthalmologists [15,25,28]. By providing depth-resolved imaging capability, OCTA allows high resolution visualization of micro vasculatures in the retina [29,30]. Quantitative features, such as tortuosity, vessel density, etc., in OCTA have been used for evaluating DR [31,32], SCR [33,34], etc.,. However, quantitative analysis of vessel angle analysis is not yet established. In this study, we demonstrated quantitative analysis of VBA automatically. To further quantify the bifurcation, the automated algorithm could also quantify individual angles of the child vessels, i.e., CBA1 and CBA2, to evaluate the orientation changes from the parent vessel direction. We observed that VBA ( $\theta$ ), CBA1 ( $\alpha_1$ ), and CBA2 ( $\alpha_2$ ) increased. This indicates that both vessels contribute to the widening of the total VBA.

Similarly, width-based features, such as VBC, also reflect transport optimality in retinal vasculature. Vessel width is related to the vessel cross sectional area and volume, and changes to the vessel width will affect the flow of blood and nutrients. Quantitative OCTA analysis of vessel caliber has been demonstrated [31,32]. However, comprehensive analysis of vessel branching properties is not yet validated. In this study, we verified VBC as a sensitive biomarker to DR detection and staging classification. By using ratio parameter VBC, the effect of image size and scale on quantitative measurement can be minimized. We also measured VWR1 and VWR2, width ratios of the individual child vessels to the width of the parent vessel, to provide further information such as contraction or dilation of child vessels. Based on the report by Adam et. al. [35], symmetrical bifurcations should have a branching coefficient of 1.26, and in case of non-symmetrical bifurcations, the VBC decrease from this optimal value. In our study, we observed that healthy control subjects had an average VBC of 1.20, close to the theoretical optimal value. We also observed that the VBC decreases in DR patients compared to healthy control patients. Similarly, we observed decreased VWR1 and VWR2 values in DR patients. We speculate the decreased vessel widths and increased vessel branching angles are possibly due to remodeling related to ischemia and neovascularization. This remodeling could increase the shear stress at bifurcations resulting in increased vessel branching angles. Further functional imaging study of retinal hemodynamics may provide insights to a better understanding of these geometric parameter changes.

It was observed that for NPDR, VBA widens from mild to moderate groups, but then narrows from moderate to severe (Table 3). This observation is consistent to previous study with traditional fundus photography [26]. Interestingly, we observed that VBA decreases from control to NoDR (Table 3), then increases from NoDR to moderate, and then decreases once more from moderate to severe. This phenomenon might reflect an auto-regulatory response due to increased metabolic demand in NoDR groups. Jiang et. al. [36] recently observed a similar trend in retinal thickness in NoDR OCT. These unique OCTA features might reflect subtle vascular abnormalities that cannot be revealed in traditional fundus photography.

## 5. Conclusion

In conclusion, an automated algorithm was developed to quantify six geometric features, including VBA ( $\theta$ ), CBA1 ( $\alpha_1$ ), CBA2 ( $\alpha_2$ ), VBC, VWR1, and VWR2. Comparative analysis of healthy control, diabetes with NoDR and DR subjects revealed that the VBA, CBA1 ( $\alpha_1$ ), VBC, and VWR1 showed significant difference among control, NoDR and NPDR groups. The study demonstrates the potential of using quantitative geometric features as objective biomarker for DR detection, progression monitoring, and treatment assessment.

## Funding

National Institutes of Health (R01 EY023522, R01 EY024628, P30 EY001792); Research to Prevent Blindness; Richard and Loan Hill Endowment; Marion H. Schenk Endowment.

## Disclosures

No conflict of interest for any authors.

## References

1. "National Eye Institute [Internet]. Bethesda (MD): National Institutes of Health (US); Facts About Diabetic Eye Disease; reviewed 2015 September; cited 2019 January 16. Available from: <https://nei.nih.gov/health/diabetic/retinopathy>", retrieved.
2. M. K. Ikram, C. Y. Cheung, M. Lorenzi, R. Klein, T. L. Jones, and T. Y. Wong; NIH/JDRF Workshop on Retinal Biomarker for Diabetes Group, "Retinal vascular caliber as a biomarker for diabetes microvascular complications," *Diabetes Care* **36**(3), 750–759 (2013).
3. C. D. Murray, "The physiological principle of minimum work: I. The vascular system and the cost of blood volume," *Proc. Natl. Acad. Sci. U.S.A.* **12**(3), 207–214 (1926).
4. C. Y. Cheung, M. K. Ikram, R. Klein, and T. Y. Wong, "The clinical implications of recent studies on the structure and function of the retinal microvasculature in diabetes," *Diabetologia* **58**(5), 871–885 (2015).
5. J. E. Grunwald, J. DuPont, and C. E. Riva, "Retinal haemodynamics in patients with early diabetes mellitus," *Br. J. Ophthalmol.* **80**(4), 327–331 (1996).
6. G. Leontidis, B. Al-Diri, and A. Hunter, "Diabetic retinopathy: current and future methods for early screening from a retinal hemodynamic and geometric approach," *Expert Rev. Ophthalmol.* **9**(5), 431–442 (2014).
7. M. B. Sasongko, J. J. Wang, K. C. Donaghue, N. Cheung, P. Benitez-Aguirre, A. Jenkins, W. Hsu, M.-L. Lee, and T. Y. Wong, "Alterations in retinal microvascular geometry in young type 1 diabetes," *Diabetes Care* **33**(6), 1331–1336 (2010).
8. P. Benitez-Aguirre, M. E. Craig, M. B. Sasongko, A. J. Jenkins, T. Y. Wong, J. J. Wang, N. Cheung, and K. C. Donaghue, "Retinal vascular geometry predicts incident retinopathy in young people with type 1 diabetes: a prospective cohort study from adolescence," *Diabetes Care*, DC\_102419 (2011).
9. L. S. Lim, M. L. Chee, C. Y. Cheung, and T. Y. Wong, "Retinal vessel geometry and the incidence and progression of diabetic retinopathy," *Invest. Ophthalmol. Vis. Sci.* **58**(6), BIO200 (2017).
10. C. Y. Cheung, C. Sabanayagam, A. K. Law, N. Kumari, D. S. Ting, G. Tan, P. Mitchell, C. Y. Cheng, and T. Y. Wong, "Retinal vascular geometry and 6 year incidence and progression of diabetic retinopathy," *Diabetologia* **60**(9), 1770–1781 (2017).
11. R. Klein, K. E. Lee, L. Danforth, M. Y. Tsai, R. E. Gangnon, S. E. Meuer, T. Y. Wong, C. Y. Cheung, and B. E. Klein, "The Relationship of Retinal Vessel Geometric Characteristics to the Incidence and Progression of Diabetic Retinopathy," *Ophthalmology* **125**(11), 1784–1792 (2018).
12. H. Lee, M. Lee, H. Chung, and H. C. Kim, "Quantification of retinal vessel tortuosity in diabetic retinopathy using optical coherence tomography angiography," *Retina* **38**(5), 976–985 (2018).
13. R. Crosby-Nwaobi, L. Z. Heng, and S. Sivaprasad, "Retinal vascular calibre, geometry and progression of diabetic retinopathy in type 2 diabetes mellitus," *Ophthalmologica* **228**(2), 84–92 (2012).
14. G. Leontidis, B. Al-Diri, J. Wigdahl, and A. Hunter, "Evaluation of geometric features as biomarkers of diabetic retinopathy for characterizing the retinal vascular changes during the progression of diabetes," in (IEEE Engineering in Medicine and Biology Society, 2015).
15. M. S. Habib, B. Al-Diri, A. Hunter, and D. H. Steel, "The association between retinal vascular geometry changes and diabetic retinopathy and their role in prediction of progression--an exploratory study," *BMC Ophthalmol.* **14**(1), 89 (2014).
16. T. T. Nguyen and T. Y. Wong, "Retinal vascular changes and diabetic retinopathy," *Curr. Diab. Rep.* **9**(4), 277–283 (2009).
17. A. Avakian, R. E. Kalina, E. H. Sage, A. H. Rambhia, K. E. Elliott, E. L. Chuang, J. I. Clark, J.-N. Hwang, and P. Parsons-Wingerter, "Fractal analysis of region-based vascular change in the normal and non-proliferative diabetic retina," *Curr. Eye Res.* **24**(4), 274–280 (2002).

18. M. S. Roy, R. Klein, and M. N. Janal, "Retinal venular diameter as an early indicator of progression to proliferative diabetic retinopathy with and without high-risk characteristics in African Americans with type 1 diabetes mellitus," *Arch. Ophthalmol.* **129**(1), 8–15 (2011).
19. N. Chapman, A. Mohamudally, A. Cerutti, A. Stanton, A. A. Sayer, C. Cooper, D. Barker, A. Rauf, J. Evans, R. Wormald, P. Sever, A. Hughes, and S. Thom, "Retinal vascular network architecture in low-birth-weight men," *J. Hypertens.* **15**(12 Pt 1), 1449–1453 (1997).
20. N. Patton, A. Pattie, T. MacGillivray, T. Aslam, B. Dhillon, A. Gow, J. M. Starr, L. J. Whalley, and I. J. Deary, "The association between retinal vascular network geometry and cognitive ability in an elderly population," *Invest. Ophthalmol. Vis. Sci.* **48**(5), 1995–2000 (2007).
21. S. Zahid, R. Dolz-Marco, K. B. Freund, C. Balaratnasingam, K. Dansingani, F. Gilani, N. Mehta, E. Young, M. R. Klifto, B. Chae, L. A. Yannuzzi, and J. A. Young, "Fractal Dimensional Analysis of Optical Coherence Tomography Angiography in Eyes With Diabetic Retinopathy," *Invest. Ophthalmol. Vis. Sci.* **57**(11), 4940–4947 (2016).
22. B. I. Gramatikov, "Modern technologies for retinal scanning and imaging: an introduction for the biomedical engineer," *Biomed. Eng. Online* **13**(1), 52 (2014).
23. K. R. Mendis, C. Balaratnasingam, P. Yu, C. J. Barry, I. L. McAllister, S. J. Cringle, and D.-Y. Yu, "Correlation of histologic and clinical images to determine the diagnostic value of fluorescein angiography for studying retinal capillary detail," *Invest. Ophthalmol. Vis. Sci.* **51**(11), 5864–5869 (2010).
24. S.-C. Cheng and Y.-M. Huang, "A novel approach to diagnose diabetes based on the fractal characteristics of retinal images," *IEEE Trans. Inf. Technol. Biomed.* **7**(3), 163–170 (2003).
25. T. Luo, T. J. Gast, T. J. Vermeer, and S. A. Burns, "Retinal Vascular Branching in Healthy and Diabetic Subjects," *Invest. Ophthalmol. Vis. Sci.* **58**(5), 2685–2694 (2017).
26. M. N. Ahmadabadi, F. S. Rooholamini, M. R. Esfahani, R. Karkhaneh, M. Nikdel, and E. N. Ahmadabadi, "Association of Retinal Vascular Diameter and Vascular Branching Angle with Diabetic Retinopathy Stage: A Cross-Sectional Study," *Iran. J. Ophthalmol.* **23**, 21 (2011).
27. N. M. Bates, J. Tian, W. E. Smiddy, W.-H. Lee, G. M. Somfai, W. J. Feuer, J. C. Shiffman, A. E. Kuriyan, N. Z. Gregori, M. Kostic, S. Pineda, and D. Cabrera DeBuc, "Relationship between the morphology of the foveal avascular zone, retinal structure, and macular circulation in patients with diabetes mellitus," *Sci. Rep.* **8**(1), 5355 (2018).
28. B. Al-Diri, A. Hunter, D. Steel, and M. Habib, "Manual measurement of retinal bifurcation features," in *Engineering in Medicine and Biology Society (EMBC), 2010 Annual International Conference of the IEEE*, (IEEE, 2010), 4760–4764.
29. Q. Zhang, K. A. Rezaei, S. S. Saraf, Z. Chu, F. Wang, and R. K. Wang, "Ultra-wide optical coherence tomography angiography in diabetic retinopathy," *Quant. Imaging Med. Surg.* **8**(8), 743–753 (2018).
30. Y. Lu, J. M. Simonett, J. Wang, M. Zhang, T. Hwang, A. M. Hagag, D. Huang, D. Li, and Y. Jia, "Evaluation of Automatically Quantified Foveal Avascular Zone Metrics for Diagnosis of Diabetic Retinopathy Using Optical Coherence Tomography Angiography," *Invest. Ophthalmol. Vis. Sci.* **59**(6), 2212–2221 (2018).
31. M. Alam, Y. Zhang, J. I. Lim, R. V. P. Chan, M. Yang, and X. Yao, "Quantitative OCT angiography features for objective classification and staging of diabetic retinopathy," *RETINA The Journal of Retinal and Vitreous Diseases*. In press.
32. M. Ashraf, P. L. Nesper, L. M. Jampol, F. Yu, and A. A. Fawzi, "Statistical Model of Optical Coherence Tomography Angiography Parameters That Correlate With Severity of Diabetic Retinopathy," *Invest. Ophthalmol. Vis. Sci.* **59**(10), 4292–4298 (2018).
33. M. Alam, D. Thapa, J. I. Lim, D. Cao, and X. Yao, "Computer-aided classification of sickle cell retinopathy using quantitative features in optical coherence tomography angiography," *Biomed. Opt. Express* **8**(9), 4206–4216 (2017).
34. M. Alam, D. Thapa, J. I. Lim, D. Cao, and X. Yao, "Quantitative characteristics of sickle cell retinopathy in optical coherence tomography angiography," *Biomed. Opt. Express* **8**(3), 1741–1753 (2017).
35. J. A. Adam, "Blood vessel branching: beyond the standard calculus problem," *Math. Mag.* **84**(3), 196–207 (2011).
36. J. Jiang, Y. Liu, Y. Chen, B. Ma, Y. Qian, Z. Zhang, D. Zhu, Z. Wang, and X. Xu, "Analysis of changes in retinal thickness in type 2 diabetes without diabetic retinopathy," *J. Diabetes Res.* **2018**, 3082893 (2018).